

# Microscopic Study of Atomic Layer Deposition of TiO<sub>2</sub> on GaAs and Its Photocatalytic Application

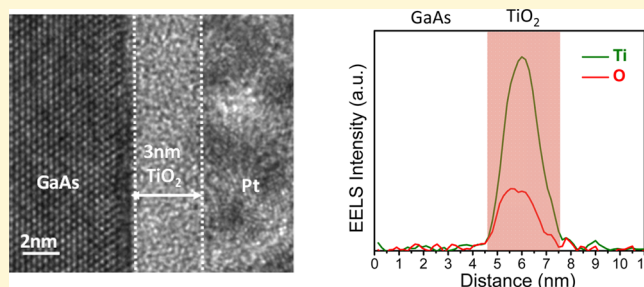
Jing Qiu,<sup>†</sup> Guangtong Zeng,<sup>§</sup> Mai-Anh Ha,<sup>||</sup> Bingya Hou,<sup>‡</sup> Matthew Mecklenburg,<sup>¶</sup> Haotian Shi,<sup>§</sup> Anastassia N. Alexandrova,<sup>||,⊥</sup> and Stephen B. Cronin<sup>\*,‡,§</sup>

<sup>†</sup>Department of Materials Science, <sup>‡</sup>Department of Electrical Engineering, <sup>§</sup>Department of Chemistry, and <sup>¶</sup>Center for Electron Microscopy and Microanalysis, University of Southern California, Los Angeles, California 90089, United States

<sup>||</sup>Department of Chemistry and Biochemistry and <sup>⊥</sup>California NanoSystems Institute, University of California Los Angeles, Los Angeles, California 90025, United States

## Supporting Information

**ABSTRACT:** We report a microscopic study of *p*-GaAs/TiO<sub>2</sub> heterojunctions using cross-sectional high resolution transmission electron microscopy (HRTEM). The photocatalytic performance for both H<sub>2</sub> evolution and CO<sub>2</sub> reduction of these heterostructures shows a very strong dependence on the thickness of the TiO<sub>2</sub> over the range of 0–15 nm. Thinner films (1–10 nm) are amorphous and show enhanced catalytic performance with respect to bare GaAs. HRTEM images and electron energy loss spectroscopy (EELS) maps show that the native oxide of GaAs is removed by the TiCl<sub>4</sub> atomic layer deposition (ALD) precursor, which is corrosive. Ti<sup>3+</sup> defect states (i.e., O vacancies) in the TiO<sub>2</sub> film provide catalytically active sites, which improve the photocatalytic efficiency. Density functional theory (DFT) calculations show that water molecules and CO<sub>2</sub> molecules bind stably to these Ti<sup>3+</sup> states. Thicker TiO<sub>2</sub> films (15 nm) are crystalline and have poor charge transfer due to their insulating nature, while thinner amorphous TiO<sub>2</sub> films are conducting.



Since Fujishima and Honda initially demonstrated photocatalytic water splitting using TiO<sub>2</sub> in 1972,<sup>1</sup> the study of photocatalysis has received worldwide interest due to its potential applications in solar fuel generation either through water splitting or CO<sub>2</sub> reduction. While TiO<sub>2</sub> is a widely studied material, its theoretical photocurrent density under one-sun illumination is only about 1–2 mA/cm<sup>2</sup>. Narrower band gap materials like Si, InP, and GaAs are more promising candidates, since their theoretical photocurrent densities are 44, 35, and 32 mA/cm<sup>2</sup>, respectively.<sup>2</sup> However, one of the primary problems, which prevents these narrower band gap materials from being utilized as photocatalysts, is that their surfaces are not photochemically stable.<sup>3</sup> Therefore, passivating their surfaces to protect them from photocorrosion without sacrificing their photoconversion efficiency will enable more efficient photocatalytic systems to be developed.

Recently, several groups have demonstrated that a very thin layer of TiO<sub>2</sub> can be used to make these narrower band gap materials stable. Chen et al. first showed that TiO<sub>2</sub> deposited by atomic layer deposition (ALD) can stabilize silicon photoanodes for water oxidation.<sup>4</sup> Hu et al. also reported that amorphous TiO<sub>2</sub> coatings stabilize Si, GaAs, and GaP photoanodes for efficient water oxidation.<sup>5</sup> For the study of photocathodes, it is also reported that TiO<sub>2</sub> can be used to protect *p*-InP from corrosion and provide efficient solar-driven H<sub>2</sub> production.<sup>6,7</sup> Our group's previous work showed that, in

addition to making GaP and InP photocathodes photochemically stable, a thin layer of TiO<sub>2</sub> can also provide substantial enhancement in the photoconversion efficiency for both H<sub>2</sub> evolution and CO<sub>2</sub> reduction.<sup>8–10</sup> More recently, Lin et al. has also discussed similar enhancement in photocatalytic H<sub>2</sub> evolution using InP and TiO<sub>2</sub> films deposited with various ALD precursors, including TDMAT (i.e., [(CH<sub>3</sub>)<sub>2</sub>N]<sub>4</sub>Ti) and titanium isopropoxide (i.e., C<sub>12</sub>H<sub>28</sub>O<sub>4</sub>Ti).<sup>11</sup> While these previous works are very encouraging, a detailed microscopic picture of these TiO<sub>2</sub>-passivated heterostructures is lacking.

In this report, we provide a detailed study of TiO<sub>2</sub> layer growth on GaAs by atomic layer deposition using high resolution transmission electron microscopy (HRTEM) and electron energy-loss spectroscopy (EELS), as well as plane wave density functional theory (PW-DFT) calculations, which are carried out to provide a detailed picture of the *p*-GaAs/TiO<sub>2</sub> interface and explore the role of surface binding of reactants and intermediate species to the TiO<sub>2</sub> surface. In this work, *p*-type (111) oriented GaAs substrates with a Zn dopant concentration of 6 × 10<sup>16</sup> cm<sup>-3</sup> (obtained from University Wafer, Inc.) are used as the photocathode. There is approximately 3 nm of native oxide on the GaAs surface

Received: August 20, 2015

Revised: November 17, 2015

Published: November 17, 2015

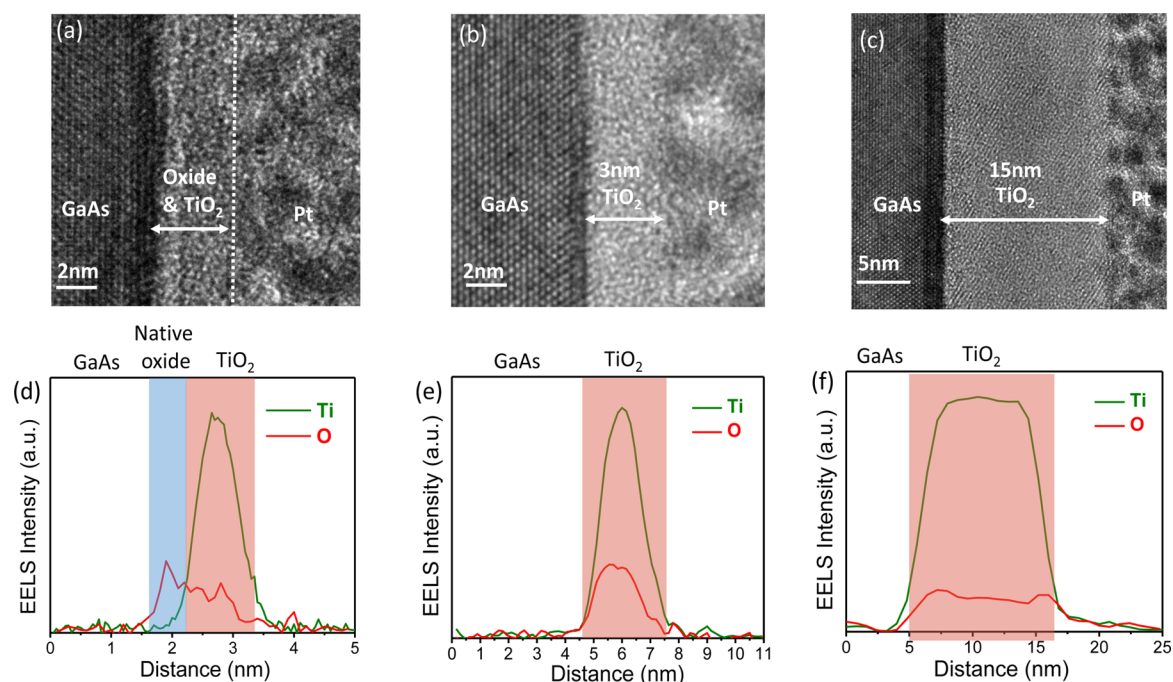


**Figure 1.** High resolution TEM image of TiO<sub>2</sub> films deposited with (a) 25 cycles, (b) 75 cycles, and (c) 500 cycles of atomic layer deposition on GaAs. Note that, for TEM sample preparation and imaging purposes, the surface of the substrate is coated with a thick layer of Pt. (d,e) EELS spatial profiles of Ti L edge (green line) and O K edge map (red line) for the 25, 75, and 500 cycle TiO<sub>2</sub> on GaAs samples, respectively.

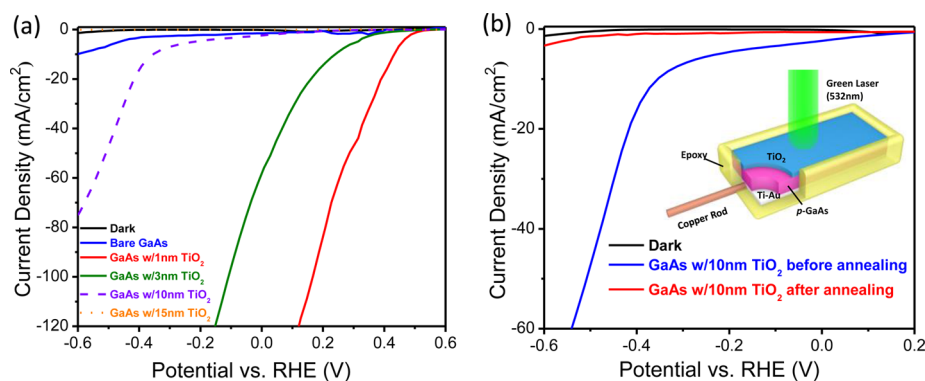


**Figure 2.** Photocatalytic water splitting current–potential curves for samples of (a) GaAs photocatalysts with various thicknesses of TiO<sub>2</sub> and (b) GaAs with 10 nm TiO<sub>2</sub> before and after annealing under 532 nm illumination in a 0.5 M H<sub>2</sub>SO<sub>4</sub> pH = 0 solution. The dark curves are for bare GaAs. Inset shows schematic diagram of the GaAs/TiO<sub>2</sub> sample geometry.

(Figure S1). Atomic layer deposition of TiO<sub>2</sub> was performed at 250 °C on the *p*-GaAs wafers using TiCl<sub>4</sub> as the titanium source and water vapor as the oxygen source. TiCl<sub>4</sub> is used for the first half-cycle, and argon was the carrier gas with a flow rate of 20 sccm during deposition. Figure 1a–c shows HRTEM images of TiO<sub>2</sub> films deposited with 25, 75, and 500 cycles of atomic layer deposition on GaAs. These films have nominal thicknesses of 1, 3, and 15 nm, respectively. Pt was deposited in order to enable cross section sample preparation using focused ion beam milling and was not used in the photocatalysis measurements described below. Figure 1d–f shows EELS spatial profiles of the Ti and O species for the 25, 75, and 500 cycle TiO<sub>2</sub> on GaAs samples, respectively. In Figure 1d, the oxygen signal increases approximately 0.5 nm before the Ti signal, indicating the presence of the GaAs native oxide underneath the TiO<sub>2</sub> layer. Therefore, on the basis of these EELS spectra, there is both native GaAs oxide and amorphous TiO<sub>2</sub> on the GaAs surface after the 25 cycle ALD process. It should be noted that the

thickness of GaAs's native oxide is substantially lower than the 3 nm native oxide observed on bare GaAs (without TiO<sub>2</sub> deposition), as shown in the inset diagram in Figure 2b. After 25 ALD cycles, the native oxide of the GaAs was partially removed due to the Cl<sup>−</sup> ions from the TiCl<sub>4</sub> precursor. Figure 1e shows the EELS spatial maps of GaAs with 75 cycles of atomic layer deposition of TiO<sub>2</sub>. Here, both the O and Ti signals increase together, indicating that the native oxide of GaAs has been completely removed during the ALD process. With further growth of 500 cycles, the amorphous TiO<sub>2</sub> becomes crystalline as shown in Figure 1f. This layer of TiO<sub>2</sub> is in the anatase phase with clear lattice planes along the 101 direction, identified by the interplane distance of  $3.5 \pm 0.1$  Å, as indicated in Figure S2. Shi et al.'s work also shows anatase phase TiO<sub>2</sub> formed by high temperature atomic layer deposition.<sup>12</sup>

Figure 2a shows the H<sub>2</sub> evolution photocurrent–voltage curves of *p*-GaAs photocathodes with various thicknesses of

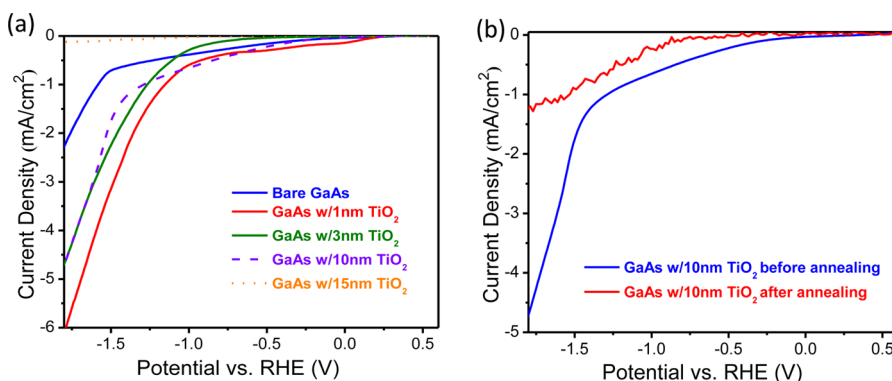


**Figure 3.** Photocatalytic CO<sub>2</sub> reduction current–potential curves for samples of (a) GaAs photocatalysts with various thicknesses of TiO<sub>2</sub> and (b) GaAs with 10 nm TiO<sub>2</sub> before and after annealing under 532 nm illumination in a 0.02 M [EMIM]BF<sub>4</sub> nonaqueous CO<sub>2</sub> saturated electrolyte.

TiO<sub>2</sub> under 910 mW/cm<sup>2</sup> 532 nm illumination in a 0.5 M H<sub>2</sub>SO<sub>4</sub> electrolyte, plotted together with bare GaAs. The bare GaAs (blue curve) exhibits an onset of photocurrent at a potential of approximately −0.05 V vs RHE. The TiO<sub>2</sub>-passivated GaAs shows a clear shift in the onset potential. The sample with a nominal thickness of 1 nm TiO<sub>2</sub> exhibits the most prominent shift, lowering the overpotential from −0.75 V (blue curve) to 0.32 V (at 10 mA/cm<sup>2</sup>) (red curve) with a 120×-fold enhancement of photocurrent over bare GaAs at 0 V vs RHE. This potential shift can be seen more clearly from the log–linear plot of the photo-*I*–*V* data shown in Figure S7. These results were reproduced consistently in several different sets of samples. The enhancement is attributed to the oxygen vacancies (Ti<sup>3+</sup> states), which provide the photocatalytically active site for H<sub>2</sub> evolution, which is consistent with the results from PW-DFT calculations shown in Figure 4b. At the same time, we observe no improvement when the TiO<sub>2</sub> thickness reaches 15 nm, as shown by the orange curve. This is because amorphous TiO<sub>2</sub> is far more conductive than crystalline TiO<sub>2</sub>, which is insulating and, therefore, impedes charge transfer to the ions in solution. In the works of Chen et al.<sup>4</sup> and Viswanathan et al.,<sup>13</sup> it was assumed that electrons were tunneling through a high-quality ALD layer,<sup>13</sup> whereas in the work of Hu et al.,<sup>5</sup> it was reported that electronically leaky amorphous TiO<sub>2</sub> films enabled efficient charge transport to the ions in solution. Since then, detailed DFT calculations have established the conduction mechanism in amorphous TiO<sub>2</sub> films.<sup>14</sup> For TiO<sub>2</sub> thicknesses between 1 and 15 nm, the photocatalytic performance becomes substantially worse with increasing thickness. We believe the TiO<sub>2</sub> films become increasingly crystalline, and hence more insulating, as the thickness is increased. Figure 2b shows the photocurrent–voltage curves for 10 nm TiO<sub>2</sub> on GaAs before and after annealing. The photocurrent decreases dramatically after annealing, due to the crystallization of the TiO<sub>2</sub> during annealing, which is consistent with the result of the 15 nm crystalline TiO<sub>2</sub> film on GaAs. We also measured the photo-*I*–*V* characteristics of both etched and unetched bare GaAs (Figure S6). There is not much difference in the photo-*I*–*V* characteristics, which indicate that native oxide has a limited effect on the H<sub>2</sub> evolution reaction. The H<sub>2</sub> product was detected using gas chromatography, as shown in Figure S3a.

In addition to H<sub>2</sub> evolution, we also characterized the photocatalytic performance of these *p*-GaAs/TiO<sub>2</sub> heterostructures for CO<sub>2</sub> reduction to CO. A nonaqueous ionic liquid electrolyte was used to exclude the effect of H<sub>2</sub>O

splitting, which has a lower onset potential than CO<sub>2</sub> reduction and tends to dominate the Faradaic efficiency. Figure 3a shows the photocurrent–voltage curves for GaAs passivated with various thicknesses of TiO<sub>2</sub> measured in an AcN electrolyte with 0.02 M [EMIM]BF<sub>4</sub> under 532 nm wavelength illumination. During these measurements, CO<sub>2</sub> is continuously bubbled through the solution. For TiO<sub>2</sub> thicknesses up to 10 nm, TiO<sub>2</sub>-passivated GaAs samples exhibit a higher photocurrent than bare GaAs (blue curve). Also, clear shifts in the onset potential required to initiate this reaction can also be seen in the *I*–*V* characteristics of samples passivated with TiO<sub>2</sub>, which is consistent with the predictions of the PW-DFT calculations discussed below. Again, we observed no improvement when the TiO<sub>2</sub> thickness reaches 15 nm, as shown in the orange curve, due to its insulating crystalline nature. Figure 3b shows the photocurrent–voltage curves for 10 nm TiO<sub>2</sub> on GaAs before and after annealing. The photocurrent decreases dramatically after annealing, which is due to the crystallization of TiO<sub>2</sub> during annealing. Photocatalytic production of CO from CO<sub>2</sub> reduction was analyzed using gas chromatography, as shown in Figure S3b.

It is widely accepted that the reduction of H<sub>2</sub>O to form H<sub>2</sub> occurs predominantly at the Ti<sup>3+</sup>-O vacancy sites due to the reaction of adsorbed H<sup>+</sup> ions.<sup>15,16</sup> Thus, a higher concentration of O vacancies correspond to more active sites, resulting in a higher hydrogen generation efficiency. Similarly, these Ti<sup>3+</sup>-O vacancy sites can also provide the catalytically active sites for CO<sub>2</sub> reduction.<sup>17–19</sup> As was previously done,<sup>20</sup> plane wave density functional theory (PW-DFT) calculations were performed on a supercell of anatase composed of 16 TiO<sub>2</sub> units exposing the 101 surface. The Quantum Espresso package was used with the most recently available ultrasoft pseudopotentials with scalar relativistic corrections,<sup>21–24</sup> and spin-unrestricted calculations were done employing the Perdew–Burke–Ernzerhof (PBE) functional.<sup>25</sup> Kinetic energy cutoffs of 435.2 (4.352) eV were applied to the wave functions (charge density) with a 1 × 1 × 1 Monkhorst-Pack k-point grid centered at  $\Gamma$ . A DFT+D+U approach was instituted with Grimme’s method<sup>26</sup> for dispersion forces (+D) and a Hubbard *U* parameter of 3.6 eV (+U). An explanation for this approach was provided in our previous study.<sup>20</sup> Clean, stoichiometric anatase and defective anatase with a surface oxygen vacancy were both investigated in this study. Adsorption energies were calculated by subtracting energies of the two components (H<sub>2</sub>O and surface) from the energy of the adsorbed system:

$$E_{\text{ads}} = E[\text{surf} + \text{H}_2\text{O}] - E[\text{surf}] - E[\text{H}_2\text{O}]$$

where the surface was stoichiometric anatase or defective anatase with a surface oxygen vacancy.

A manual search was performed to determine the global minimum of adsorbed H<sub>2</sub>O to the anatase support reproducing the same geometries found in Tilocca et al.'s study on water on anatase.<sup>27</sup> Adsorption energies were favorable between neutral H<sub>2</sub>O adsorbed to stoichiometric (−1.26 eV as indicated in Figure S5) and defective anatase (−1.50 eV). These energies differ from those of Tilocca et al. due to possible interactions across our smaller supercell and the additional consideration of dispersion forces, which lowered the adsorption to stoichiometric anatase significantly (Tilocca et al. reported −0.74 eV) and to defective anatase minimally (Tilocca et al. reported −1.48 eV). As in our findings with CO<sub>2</sub>, molecules adsorbed to defective anatase tend to fill the surface oxygen vacancy. In Figure 4b, the water molecule attempts to both fill the oxygen

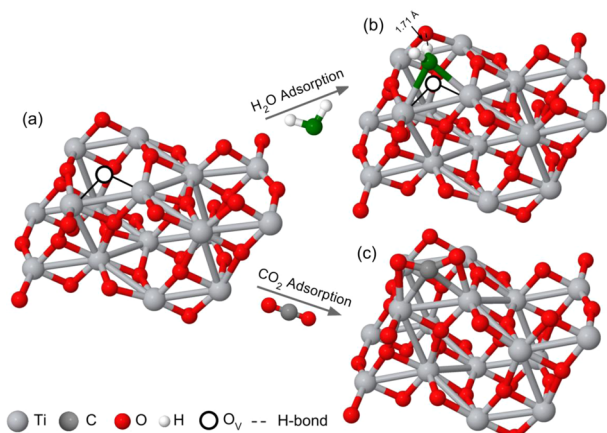


**Figure 4.** PW-DFT calculated structure for anatase TiO<sub>2</sub> with O vacancies (a) before adsorption, (b) after H<sub>2</sub>O adsorption and relaxation, and (c) after CO<sub>2</sub> adsorption and relaxation.

vacancy with its oxygen (colored green) and retain a hydrogen bond to the neighboring surface oxygen on the oxide support. Moreover, the hydrogen bond might be considered an “activated” bond with a length of 1.71 Å as compared to 1.89 Å on the stoichiometric support, indicating that the system is approaching the proton transfer to the O atom of the support. In a molecular dynamics study, Tilocca et al. estimated the activation barrier from adsorption of H<sub>2</sub>O to dissociation of the H<sub>2</sub>O to two hydroxyls to be ~0.1 eV.<sup>28</sup> Moreover, Fujimori et al. maintained that hydroxylation of their MgO support provided the pathway for two mechanisms of hydrogen evolution: the direct redox process and the water–gas shift reaction in the presence of CO.<sup>29</sup> This indicates that Ti<sup>3+</sup>-O sites are more energetically favorable for H<sub>2</sub>O adsorption, which results in higher H<sub>2</sub> evolution efficiencies, consistent with previous reports in the literature.<sup>16</sup> This calculation combined with our previous finding<sup>20</sup> of spontaneous CO<sub>2</sub> reduction on defective anatase (a charge transfer of 0.897 *e* from the support to CO<sub>2</sub>) indicates that the O vacancies provide catalytically active sites for CO<sub>2</sub> and H<sub>2</sub>O absorption, and no overpotential is required to form the CO<sub>2</sub><sup>−</sup> intermediate.

In conclusion, we have carried out a microscopic study of GaAs photocathodes passivated with various thicknesses of TiO<sub>2</sub> using atomic layer deposition. High resolution transmission electron microscopy (HRTEM) and electron energy-loss spectroscopy (EELS) show that the native oxide of GaAs is

removed by the TiCl<sub>4</sub> precursor during the TiO<sub>2</sub> growth. The photocatalytic performance for both H<sub>2</sub> evolution and CO<sub>2</sub> reduction of these heterostructures shows a very strong dependence on the thickness of the TiO<sub>2</sub> over the range of 0–15 nm. Thinner TiO<sub>2</sub> films are amorphous and show enhanced catalytic performance with respect to bare GaAs, whereas thicker TiO<sub>2</sub> films (15 nm) are single crystal and have poor charge transfer due to the insulating nature of crystalline TiO<sub>2</sub>. DFT calculations show that the water and CO<sub>2</sub> molecules bind stably to TiO<sub>2</sub>, which can further improve the photocatalytic charge transfer process.

## EXPERIMENTAL METHODS

Ohmic back contacts were made for the *p*-GaAs by evaporating 5 nm of Ti followed by 50 nm of Au. The Ti–Au film was then connected to the external circuitry with a copper wire and coated with epoxy cement to insulate it from the electrolytic solution, as illustrated in the inset diagram in Figure 2b. High resolution transmission electron microscope images of TiO<sub>2</sub> on GaAs were taken with a JEOL JEM-2100F TEM equipped with a Gatan Quantum SE GIF quantum energy filter. A layer of Pt was deposited on the surfaces of samples as part of the cross section sample preparation using standard focused ion beam sample preparation techniques. TiO<sub>2</sub> films were annealed in a furnace at 450 °C for 30 min while flowing N<sub>2</sub> gas. The photocatalytic H<sub>2</sub> evolution measurements were carried out in a pH = 0 solution of 0.5 M H<sub>2</sub>SO<sub>4</sub> using a three-terminal potentiostat with the prepared samples, a Ag/AgCl electrode, and a graphite electrode functioning as the working, reference, and counter electrodes, respectively. The area of the exposed electrode surface is about 0.1 cm<sup>2</sup>. A 532 nm continuous-wave laser was used to excite the samples, and low to moderate power excitation (910 mW/cm<sup>2</sup>) was used to avoid optical heating. The nonaqueous solution (for CO<sub>2</sub> reduction) was prepared using acetonitrile (AcN, 99.99%), dimethyl sulfoxide (DMSO, 99.96% D, Sigma-Aldrich), and 1-ethyl-3-methylimidazolium tetrafluoroborate ([EMIM]BF<sub>4</sub>, 99.0%, HPLC, Sigma-Aldrich). An anion exchange membrane (Selemion AMV, Anion Exchange Membrane, AGC Inc.) was used to separate the working and counter electrodes to prevent oxidation of the reduced CO<sub>2</sub> products. This anion exchange membrane only allows negative ions to transfer through the membrane, which prevents the oxylate intermediate from participating in the oxygen evolution half-reaction at the counter electrode. A three-terminal potentiostat was used with the prepared semiconductor samples as the working electrode, a Ag/AgNO<sub>3</sub> reference electrode, and a Pt wire as the counter electrode. The Ag/AgNO<sub>3</sub> electrode was made of a silver wire immersed in 0.01 M silver nitrate dissolved in 0.1 M TEAP/AcN. Also, the reference electrode was calibrated against a ferrocene/ferrocenium (Fc<sup>+</sup>/Fc) redox couple to confirm that it gave the right potential with respect to NHE. A detailed discussion of the calibration can be found in our previous work.<sup>10</sup> Before each measurement, CO<sub>2</sub> was purged through the solution on the working electrode side for 30 min. H<sub>2</sub> evolution and the gaseous products from the CO<sub>2</sub> reduction reaction were analyzed with a gas chromatograph (GC) (Bruker GC-450) equipped with a thermal conductivity detector (TCD) and a carbon-plot column (Agilent). The produced CO was quantified by integrating the area of the CO peak, and this was related to the calibration data (Figure S4).

## ASSOCIATED CONTENT

### Supporting Information

The Supporting Information is available free of charge on the ACS Publications website at DOI: 10.1021/acs.chemmater.5b03246.

TEM images of bare GaAs and 10 nm TiO<sub>2</sub> on GaAs, gas chromatography data for product after reaction, schematic diagram of H<sub>2</sub>O adsorption on stoichiometric anatase, and additional photocatalytic current–potential curves. (PDF)

## ■ AUTHOR INFORMATION

## Notes

The authors declare no competing financial interest.

## ■ ACKNOWLEDGMENTS

This research was supported by Army Research Office Award No. W911NF-14-1-0228 (J.Q.), Air Force Office of Scientific Research Grant No. FA9550-15-1-0184 (G.Z.), and Air Force Office of Scientific Research under AFOSR BRI Grant FA9550-12-1-0481 (A.N.A.). This work used the Extreme Science and Engineering Discovery Environment (XSEDE),<sup>30</sup> which is supported by National Science Foundation Grant Number ACI-1053575.

## ■ REFERENCES

- (1) Fujishima, A.; Honda, K. Electrochemical photolysis of water at a semiconductor electrode. *Nature* **1972**, *238*, 37–38.
- (2) Liu, C.; Dasgupta, N. P.; Yang, P. Semiconductor nanowires for artificial photosynthesis. *Chem. Mater.* **2014**, *26*, 415–422.
- (3) Frese, K., Jr.; Madou, M.; Morrison, S. Investigation of photoelectrochemical corrosion of semiconductors. *J. Phys. Chem.* **1980**, *84*, 3172–3178.
- (4) Chen, Y. W.; Prange, J. D.; Dühnen, S.; Park, Y.; Gunji, M.; Chidsey, C. E.; McIntyre, P. C. Atomic layer-deposited tunnel oxide stabilizes silicon photoanodes for water oxidation. *Nat. Mater.* **2011**, *10*, 539–544.
- (5) Hu, S.; Shaner, M. R.; Beardslee, J. A.; Lichtenman, M.; Brunschwig, B. S.; Lewis, N. S. Amorphous TiO<sub>2</sub> coatings stabilize Si, GaAs, and GaP photoanodes for efficient water oxidation. *Science* **2014**, *344*, 1005–1009.
- (6) Lee, M. H.; Takei, K.; Zhang, J.; Kapadia, R.; Zheng, M.; Chen, Y. Z.; Nah, J.; Matthews, T. S.; Chueh, Y. L.; Ager, J. W.; Javey, A. p-Type InP Nanopillar Photocathodes for Efficient Solar-Driven Hydrogen Production. *Angew. Chem.* **2012**, *124*, 10918–10922.
- (7) Hettick, M.; Zheng, M.; Lin, Y. J.; Sutter-Fella, C. M.; Ager, J. W.; Javey, A. Nonepitaxial Thin-Film InP for Scalable and Efficient Photocathodes. *J. Phys. Chem. Lett.* **2015**, *6*, 2177–2182.
- (8) Qiu, J.; Zeng, G.; Pavaskar, P.; Li, Z.; Cronin, S. B. Plasmon-enhanced water splitting on TiO<sub>2</sub>-passivated GaP photocatalysts. *Phys. Chem. Chem. Phys.* **2014**, *16*, 3115–3121.
- (9) Zeng, G.; Qiu, J.; Li, Z.; Pavaskar, P.; Cronin, S. B. CO<sub>2</sub> Reduction to Methanol on TiO<sub>2</sub>-Passivated GaP Photocatalysts. *ACS Catal.* **2014**, *4*, 3512–3516.
- (10) Zeng, G.; Qiu, J.; Hou, B.; Shi, H.; Lin, Y.; Hettick, M.; Javey, A.; Cronin, S. B. Enhanced Photocatalytic Reduction of CO<sub>2</sub> to CO through TiO<sub>2</sub> Passivation of InP in Ionic Liquids. *Chem. - Eur. J.* **2015**, *21*, 13502–13507.
- (11) Lin, Y.; Kapadia, R.; Yang, J.; Zheng, M.; Chen, K.; Hettick, M.; Yin, X.; Battaglia, C.; Sharp, I. D.; Ager, J. W.; Javey, A. Role of TiO<sub>2</sub> Surface Passivation on Improving the Performance of p-InP Photocathodes. *J. Phys. Chem. C* **2015**, *119*, 2308–2313.
- (12) Shi, J.; Li, Z.; Kvit, A.; Krylyuk, S.; Davydov, A. V.; Wang, X. Electron Microscopy Observation of TiO<sub>2</sub> Nanocrystal Evolution in High-Temperature Atomic Layer Deposition. *Nano Lett.* **2013**, *13*, 5727–5734.
- (13) Viswanathan, V.; Pickrahn, K. L.; Luntz, A. C.; Bent, S. F.; Nørskov, J. K. Nanoscale Limitations in Metal Oxide Electrocatalysts for Oxygen Evolution. *Nano Lett.* **2014**, *14*, 5853–5857.
- (14) Pham, H. H.; Wang, L. W. Electronic structures and current conductivities of B, C, N and F defects in amorphous titanium dioxide. *Phys. Chem. Chem. Phys.* **2015**, *17*, 11908–11913.
- (15) Pan, J. M.; Maschhoff, B.; Diebold, U.; Madey, T. Interaction of water, oxygen, and hydrogen with TiO<sub>2</sub> (110) surfaces having different defect densities. *J. Vac. Sci. Technol., A* **1992**, *10*, 2470–2476.
- (16) Lu, G.; Linsebigler, A.; Yates, J. T., Jr. Ti<sup>3+</sup> defect sites on TiO<sub>2</sub> (110): production and chemical detection of active sites. *J. Phys. Chem.* **1994**, *98* (45), 11733–11738.
- (17) Lindan, P.; Harrison, N.; Gillan, M.; White, J. First-principles spin-polarized calculations on the reduced and reconstructed TiO<sub>2</sub> (110) surface. *Phys. Rev. B: Condens. Matter Mater. Phys.* **1997**, *55*, 15919.
- (18) Krüger, P.; Bourgeois, S.; Domenichini, B.; Magnan, H.; Chandresris, D.; Le Fevre, P.; Flank, A.; Jupille, J.; Floreano, L.; Cossaro, A.; et al. Defect states at the TiO<sub>2</sub> (110) surface probed by resonant photoelectron diffraction. *Phys. Rev. Lett.* **2008**, *100*, 055501.
- (19) Von Oertzen, G.; Gerson, A. O deficiency in the rutile TiO<sub>2</sub> (110) surface: Ab initio quantum chemical investigation of the electronic properties. *Int. J. Quantum Chem.* **2006**, *106*, 2054–2064.
- (20) Qiu, J.; Zeng, G.; Ha, M.-A.; Ge, M.; Lin, Y.; Hettick, M.; Hou, B.; Alexandrova, A. N.; Javey, A.; Cronin, S. B. Artificial Photosynthesis on TiO<sub>2</sub>-Passivated InP Nanopillars. *Nano Lett.* **2015**, *15*, 6177–6181.
- (21) Giannozzi, P.; Baroni, S.; Bonini, N.; Calandra, M.; Car, R.; Cavazzoni, C.; Ceresoli, D.; Chiarotti, G. L.; Cococcioni, M.; Dabo, I.; et al. QUANTUM ESPRESSO: a modular and open-source software project for quantum simulations of materials. *J. Phys.: Condens. Matter* **2009**, *21*, 395502.
- (22) Kohn, W.; Sham, L. J. Self-consistent equations including exchange and correlation effects. *Phys. Rev.* **1965**, *140*, A1133.
- (23) Lee, C.; Yang, W.; Parr, R. G. Development of the Colle-Salvetti correlation-energy formula into a functional of the electron density. *Phys. Rev. B: Condens. Matter Mater. Phys.* **1988**, *37*, 785.
- (24) Burke, K.; Werschnik, J.; Gross, E. Time-dependent density functional theory: Past, present, and future. *J. Chem. Phys.* **2005**, *123*, 062206.
- (25) Perdew, J. P.; Burke, K.; Ernzerhof, M. Generalized gradient approximation made simple. *Phys. Rev. Lett.* **1996**, *77*, 3865.
- (26) Grimme, S.; Antony, J.; Ehrlich, S.; Krieg, H. A consistent and accurate ab initio parametrization of density functional dispersion correction (DFT-D) for the 94 elements H-Pu. *J. Chem. Phys.* **2010**, *132*, 154104.
- (27) Tilocca, A.; Selloni, A. Structure and reactivity of water layers on defect-free and defective anatase TiO<sub>2</sub> (101) surfaces. *J. Phys. Chem. B* **2004**, *108*, 4743–4751.
- (28) Tilocca, A.; Selloni, A. Reaction pathway and free energy barrier for defect-induced water dissociation on the (101) surface of TiO<sub>2</sub>-anatase. *J. Chem. Phys.* **2003**, *119*, 7445–7450.
- (29) Fujimori, Y.; Kaden, W. E.; Brown, M. A.; Roldan Cuenya, B.; Sterrer, M.; Freund, H.-J. Hydrogen Evolution from Metal–Surface Hydroxyl Interaction. *J. Phys. Chem. C* **2014**, *118*, 17717–17723.
- (30) Towns, J.; Cockerill, T.; Dahan, M.; Foster, I.; Gaither, K.; Grimshaw, A.; Hazlewood, V.; Lathrop, S.; Lifka, D.; Peterson, G. D.; et al. XSEDE: accelerating scientific discovery. *Comput. Sci. Eng.* **2014**, *16*, 62–74.